Desalination and Water Treatment
www.deswater.com
doi: 10.5004/dwt.2018.22689

123 (2018) 211–223
August

Evaluating the hydrothermal synthesis of quasi-one-dimensional TiO_2 nanomaterials for the photocatalysis of selected organic chemicals

Tao Peng[a,b], Jian Zhang[c], Srimanta Ray[d], Houssam Fakhouri[b], Sathyanarayanan Sevilimedu Veeravalli[e], Farzaneh Arefi-Khonsari[b,*], Jerald A. Lalman[a,*]

[a]*Department of Civil and Environmental Engineering, University of Windsor, 401 Sunset Ave., Windsor, ON N9B 3P4, Canada, Tel. +1-519-253-3000 Ext. 2519; Fax + 1-519-971-3686; email: lalman@uwindsor.ca (J.A. Lalman), Tel. +1-519-991-3709; email: Peng11a@uwindsor.ca (T. Peng)*
[b]*Laboratoire Interfaces et Systèmes Electrochimiques (LISE), Centre national de la recherche scientifique (CNRS), Sorbonne Université, F-75005 Paris, France, Tel. +33-144276815; Fax: +33-144276813; email: farzaneh.arefi@upmc.fr (F. Arefi-Khonsari), Tel. +33-673989477; email: houss.fakhouri@gmail.com (H. Fakhouri)*
[c]*State Key Laboratory of Material Processing and Die and Mould Technology, School of Materials Science and Engineering, Huazhong University of Science and Technology, Wuhan 430074, China, Tel. +86-133-4992-6268; email: zhangjian7@hust.edu.cn*
[d]*Department of Chemical Engineering, National Institute of Technology Agartala, Tripura 799055, India, Tel. +91-8974867827; email: rays.nita@gmail.com*
[e]*Civil Engineering, Kansas State University, Manhattan, KS 66506, USA, Tel. +1-785-317-5964; email: sevilim@uwindsor.ca*

Received 24 December 2017; Accepted 27 June 2018

ABSTRACT

Quasi-one-dimensional (Q1D) titanium dioxide (TiO_2) nanomaterials have attracted attention in photocatalytic applications because of their high oxidative potential coupled with increasing active sites. In this study, Q1D TiO_2 samples with different phase structure, crystal size, and specific surface area were produced using a hydrothermal method by varying the reaction conditions (temperature, alkaline concentration, and the TiO_2 precursor concentration). A three-factor three-level Box–Behnken design (BBD) with three replicates (15 conditions) at the center point was employed to evaluate and optimize the hydrothermal synthesis factors in terms of photocatalysis of rhodamine B (RhB), phenol, methyl orange, and methylene blue. The BBD demonstrated that the temperature and the NaOH concentration significantly affected the Q1D TiO_2 crystal size, phase structure, bandgap, and photocatalytic activity. A reduce temperature at 120°C and a low NaOH concentration at 5 M were favorable in producing a biphasic anatase–rutile structure with optimum photocatalytic activity. Under a higher temperature of 190°C and with ≥ 10 M NaOH concentration, the presence of TiO_2-B phase resulted in the lowest photocatalytic activity.

Keywords: TiO_2 nanomaterials; Photocatalysts; Hydrothermal synthesis; Statistical optimization; Box–Behnken design (BBD)

1. Introduction

Titanium dioxide (TiO_2) is a widely studied and efficient photocatalyst for degrading organic pollutants [1–3]. The TiO_2 photocatalytic properties are strongly dependent on properties such as phase structure, crystal size, and specific surface area (SSA) [4–6]. Structural forms such as nanoparticles, nanotubes, and nanosheets are also known to impact the photocatalytic properties [7]. Based on experimental and theoretical studies, researchers have reported the following photocatalytic activity trend: nanosheet > nanotubes > nanoparticles [7]. In studies with TiO_2 nanoparticles and quasi-one-dimensional (Q1D) TiO_2

* Corresponding author.

1944-3994/1944-3986 © 2018 Desalination Publications. All rights reserved.

nanomaterials such as nanowires, nanorods, and nanotubes [8], enhanced Q1D TiO_2 photocatalytic activity was attributed to higher SSA [9–13]. Among the different approaches used to synthesize Q1D TiO_2, the alkaline hydrothermal method is relatively simple for producing Q1D TiO_2 with higher SSAs of approximately 400 $m^2 g^{-1}$ and diameters ranging from 5 to 200 nm [14–17]. Hydrothermal synthesis factors such as reaction temperature and the TiO_2:NaOH molar ratio can significantly affect the Q1D TiO_2 phase structure, crystal size, and SSA [14,16]. However, the impact of individual factor and factors in combination on the photocatalytic characteristics of Q1D TiO_2 have not been addressed in the past studies.

Numerous studies have employed the hydrothermal processes to produce Q1D TiO_2 for photocatalytic applications [9–11,18–22]. Evidence from many studies have shown improved photocatalytic activities for Q1D TiO_2 synthesized under different hydrothermal synthesis factors when compared with TiO_2 nanoparticles [9,10,21,22]. Recently, Kuo et al. [23] reported that 1% Pt/TiO_2 nanotubes (TNTs) synthesized at a relatively low temperature were 20% more effective in producing H_2 gas from ethanol when compared with a 1% Pt/TiO_2 nanoparticle photocatalyst using ultraviolet (UV) light. Perera et al. [10] synthesized reduced graphene oxide (RGO)-TNTs composites using a one-step alkaline hydrothermal process. These researchers reported Q1D TiO_2 such as TNT were homogeneously dispersed between RGO sheets with the composites showing significant improvement in the photocatalysis of malachite green dye under UV light when compared with TiO_2 nanoparticles [10]. However, these and other researchers did not address the impact of hydrothermal synthesis factors on Q1D TiO_2 photocatalytic activities [9–11,18–23].

The first objective of this study was to employ a three-factor and three-level Box–Behnken design (BBD) to evaluate the effects of selected hydrothermal process conditions such as temperature, the NaOH concentration, and the TiO_2 precursor concentration on the photocatalytic activity of Q1D TiO_2 using rhodamine B (RhB). The second objective was to access the impact of the selected hydrothermal conditions on the crystal phase, crystal size, SSA, and bandgap. The third objective was to develop and use the BBD model to predict the optimized hydrothermal conditions for the photocatalysis of RhB. The final objective was to evaluate the photocatalysis of other organic chemicals such as phenol, methyl orange (MO), and methylene blue (MB) using the optimized Q1D TiO_2.

2. Experimental

2.1. Preparation of the Q1D nanometric TiO_2 photocatalyst

Q1D TiO_2 photocatalyst was prepared by homogeneously mixing a specified quantity of TiO_2 nanoparticles (Aeroxide TiO_2 P25, Evonik Corporation, Parsippany, New Jersey) with 70 mL of a NaOH solution. Tables 1 and 2 list the reaction temperature, NaOH concentration, and TiO_2 concentration for hydrothermal process. The mixture was poured into a 100 mL Teflon® capped container. The Teflon® container was placed into a stainless-steel bomb, capped and heated to a desired temperature for 24 h and subsequently, cooled to room temperature. The resulting product was centrifuged and rinsed with 0.1 M HCl solution. The white paste was repeatedly washed (five times) with deionized water and calcinated at 400°C for 2 h to produce Q1D TiO_2 [23]. The hydrothermal conditions for temperature, NaOH and TiO_2 concentrations are shown in Table 1.

Table 1
Levels of the selected hydrothermal synthesis factors

Levels	Factors		
	A	*B*	*C*
	T (°C)	NaOH (M)	TiO_2 ($g \cdot L^{-1}$)
–1	120	5	14
0	150	10	43
1	190	15	100

Note: *T*, NaOH, and TiO_2 represent temperature, NaOH, and TiO_2 concentration, respectively.

2.2. Characterization studies

The morphology and crystal size of the samples were recorded using scanning electron microscopy (SEM) (JEOL, Japan) and high-resolution transmission electron microscopy (HRTEM) (300 kV, JEOL 3010, Japan). X-ray diffraction (XRD) analysis of the samples was performed using an X-ray diffractometer (Rigaku, MI) equipped with Cu K_α radiation source. Raman analysis was performed using an Alpha300 RA argon laser Raman spectrometer (WITec, Germany) at an excitation wavelength set at 532 nm. UV-Vis spectra analysis was performed using a Cary 300 UV-Vis (Agilent Technologies, Santa Clara, CA). Nitrogen adsorption–desorption isotherms were determined at 77 K with a Micromeritics ASAP 2020 Brunauer–Emmett–Teller (BET) analyzer (Micromeritics Instrument, Norcross, GA).

2.3. Photocatalysis of selected organic chemicals

The photocatalytic experiments were conducted using quartz tubes (25 mm ID × 250 mm length) (Technical Glass Products Inc., Painesville, OH) sealed with aluminum crimp caps and Teflon® lined rubber septa. The sealed photocatalytic reaction tubes were placed in a modified Rayonet RPR-100 UV photocatalytic chamber (Southern New England Ultraviolet Co., Branford, CT). The chamber was installed with 16 monochromatic (300 nm) UV lamps (Southern New England Ultraviolet Co., Branford, CT) on the outer perimeter of the reactor with a rotating inner carousel as described in a previous study by Ray et al. [24]. The quartz tubes in triplicates were placed on the rotating carousel and the reaction mixture was magnetically stirred to maintain the photocatalyst in suspension, minimize particle agglomeration and mass transfer limitation. The average intensity of irradiance emitted from the lamps was 9 mW cm^{-2}. The light intensity was measured using a light intensity meter equipped with a 300 nm UV sensor (UV Process Supply, Chicago, IL). The reactor temperature was maintained at 37°C ± 2°C.

The reaction mixture consisted of 100 mg L^{-1} of the photocatalysts and a model chemical at a specific concentration.

Table 2
Design matrix for the hydrothermal synthesis factors and responses (apparent reaction rate constant) at different factor levels

Sample #	Factors			Response				Phase	Mean crystal size L (nm)
	T (°C)	NaOH (M)	TiO_2 (g L^{-1})	Apparent reaction rate constant (k) (min^{-1})					
				k_1	k_2	k_3	Average k		
1	120	5	43	0.4378	0.4137	0.4165	0.4227 ± 0.0107	A + R	9.3 ± 0.1
2	190	5	43	0.3114	0.2895	0.2897	0.2962 ± 0.0102	A	21.6 ± 0.2
3	120	15	43	0.1746	0.1734	0.1629	0.1703 ± 0.0053	A	19.7 ± 0.2
4	190	15	43	0.0938	0.0945	0.0926	0.0936 ± 0.0007	A + B	58.9 ± 0.5
5	120	10	14	0.2572	0.2565	0.265	0.2596 ± 0.0039	A	18.1 ± 0.1
6	190	10	14	0.1204	0.1196	0.1114	0.1171 ± 0.0041	A + B	46.6 ± 0.3
7	120	10	100	0.1872	0.1841	0.1783	0.1832 ± 0.0037	A	17.6 ± 0.1
8	190	10	100	0.1271	0.1287	0.1246	0.1268 ± 0.0017	A + B	48.5 ± 0.6
9	150	5	14	0.2536	0.2625	0.2546	0.2569 ± 0.0039	A	16.8 ± 0.2
10	150	15	14	0.1627	0.1649	0.1834	0.1703 ± 0.0093	A	57.7 ± 0.4
11	150	5	100	0.1975	0.2000	0.2003	0.1993 ± 0.0013	A	21.2 ± 0.2
12	150	15	100	0.1559	0.1604	0.1413	0.1525 ± 0.0081	A	18.7 ± 0.2
13	150	10	43	0.1962	0.1819	0.1939	0.1906 ± 0.0062	A	19.6 ± 0.3
14	150	10	43	0.2144	0.2058	0.1958	0.2062 ± 0.0076	A	19.7 ± 0.2
15	150	10	43	0.2192	0.2306	0.2062	0.2187 ± 0.0099	A	20.6 ± 0.2

Note: T, NaOH, and TiO_2 represent temperature, NaOH, and TiO_2 concentration. A, R, and B correspond to anatase, rutile, and TiO_2-B, respectively.

The chemicals examined in the study include RhB (95%), phenol (99.5%), MO (85%), and MB (82%). All chemicals used in the photocatalysis study were purchased from Sigma-Aldrich (ON, Canada). The concentration of RhB, MO, phenol, and MB in the reaction mixture was 10, 20, 20, and 10 mg L^{-1}, respectively. The reaction mixture (50 mL) containing a specific chemical and photocatalyst was ultrasonicated for 15 min and left under dark conditions with magnetic stirring for 1 h to establish an adsorption–desorption equilibrium. The reaction mixture in quartz tubes was thereafter exposed to UV light for a specific duration. The duration of exposure to UV was maintained at 15 min for all experiments. A fixed amount of the reaction mixture (5 mL) was withdrawn at specific time intervals (of 3–5 min). The sample was centrifuged (5,000 rpm for 10 min) and filtered using a 0.1 μm polyvinylidene difluoride filter (Sigma-Aldrich, Oakville, ON) to separate the photocatalyst from the chemical in solution. The residual chemical concentration (C) in the filtrate was determined by measuring the optical absorbance at 554, 464, and 664 nm for RhB, MO, and MB, respectively, using a UV-Vis spectrophotometer. The detection limit for RhB, MO, and MB was 1 μg L^{-1}. The residual phenol concentration was determined using a high-performance liquid chromatograph (Dionex Ultimate 3000, Sunnyvale, CA) equipped with a UV-Vis photodiode array detector set at 274 nm and configured with an Acclaim C18 – 3 μm–2.1 mm (ID) × 100 mm (length) column (Dionex, Sunnyvale, CA). The analysis was conducted at 45°C with an acetonitrile–water mixture (1:4) eluent (Fisher Scientific, Ottawa, ON) at a flow rate set at 0.4 mL min^{-1} as described in an earlier study [24]. The phenol detection limit was 5.0 μg L^{-1}. The residual concentration of the chemical was used to determine the reaction rate of decoloration or disappearance, termed hereafter as the apparent reaction rate. The apparent reaction rate was modeled using a pseudo-first-order rate equation (1) [24–27].

$$\frac{-dC}{dt} = kC \tag{1}$$

where k is the apparent reaction rate constant (min^{-1}), C is the organic chemical concentration (mg L^{-1}), and $-dC/dt$ is the pseudo-first-order reaction rate.

2.4. Experimental design and statistical analysis

A three-factor three-level BBD was used to determine the experimental conditions for hydrothermal synthesis of the Q1D TiO_2 photocatalyst capable of maximizing the apparent reaction rate constant (min^{-1}). Accordingly, the apparent reaction rate constant (min^{-1}) was selected as a response variable and RhB was selected as a model chemical for the optimization study. The hydrothermal conditions for synthesis of Q1D TiO_2, namely temperature (°C), NaOH concentration (M), and TiO_2 concentration (g L^{-1}) were the selected experimental factors for the optimization study. Each experimental factor was varied at a low level (designated as −1), a central level (designated as 0), and a high level (designated as +1) (Table 1). The method is defined with three center points and 12 experimental points with three replicates under each condition (Table 2). A full quadratic model was evaluated for the response function and the apparent reaction rate constant (min^{-1}) was analyzed statistically using Minitab 15 (Minitab Inc., State College, PA). Three experiments (triplicates) designated as #13 to #15 under the same conditions were performed at the center points to evaluate the magnitude of error in the experimental analysis.

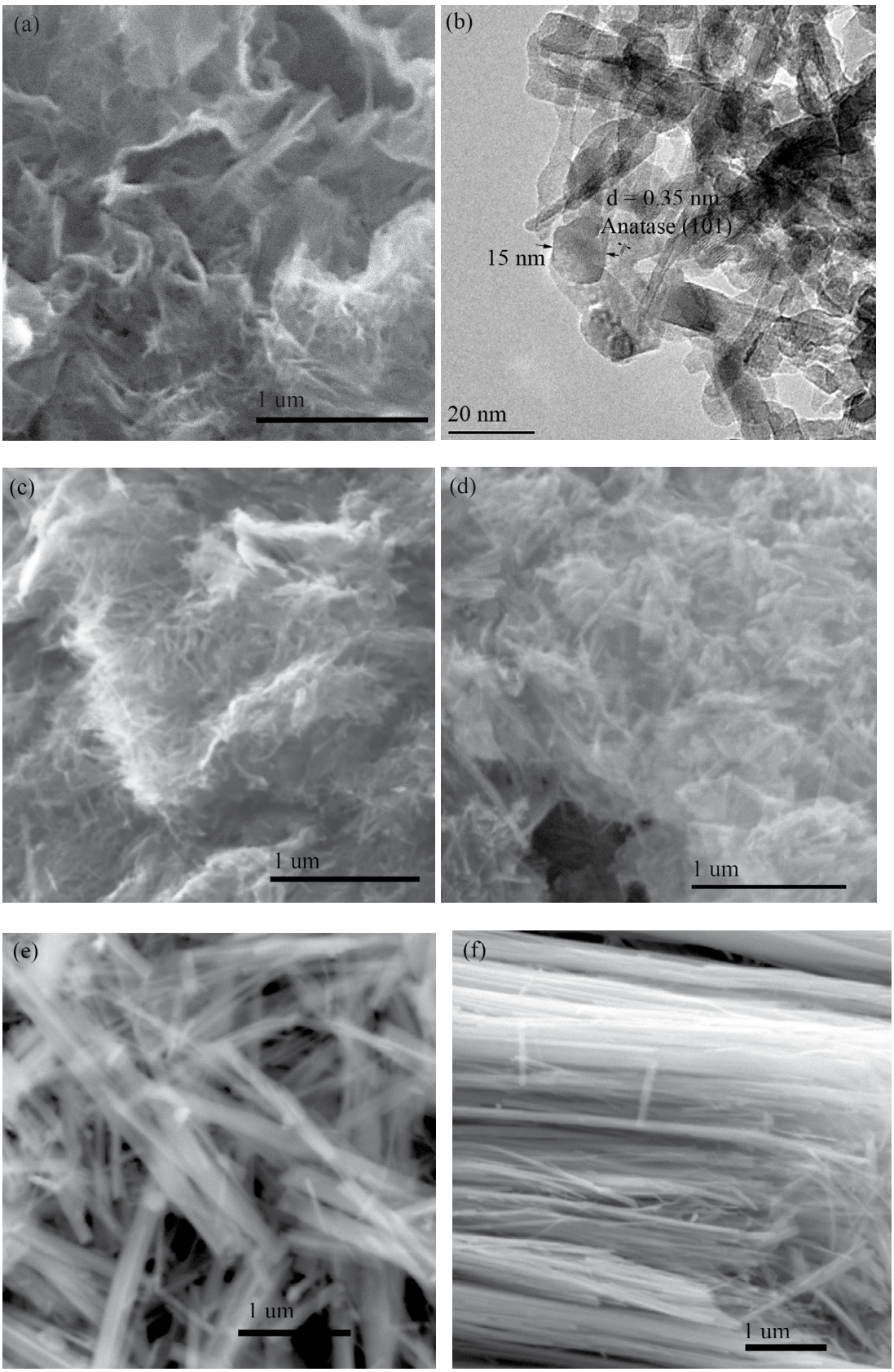

Fig. 1. continued

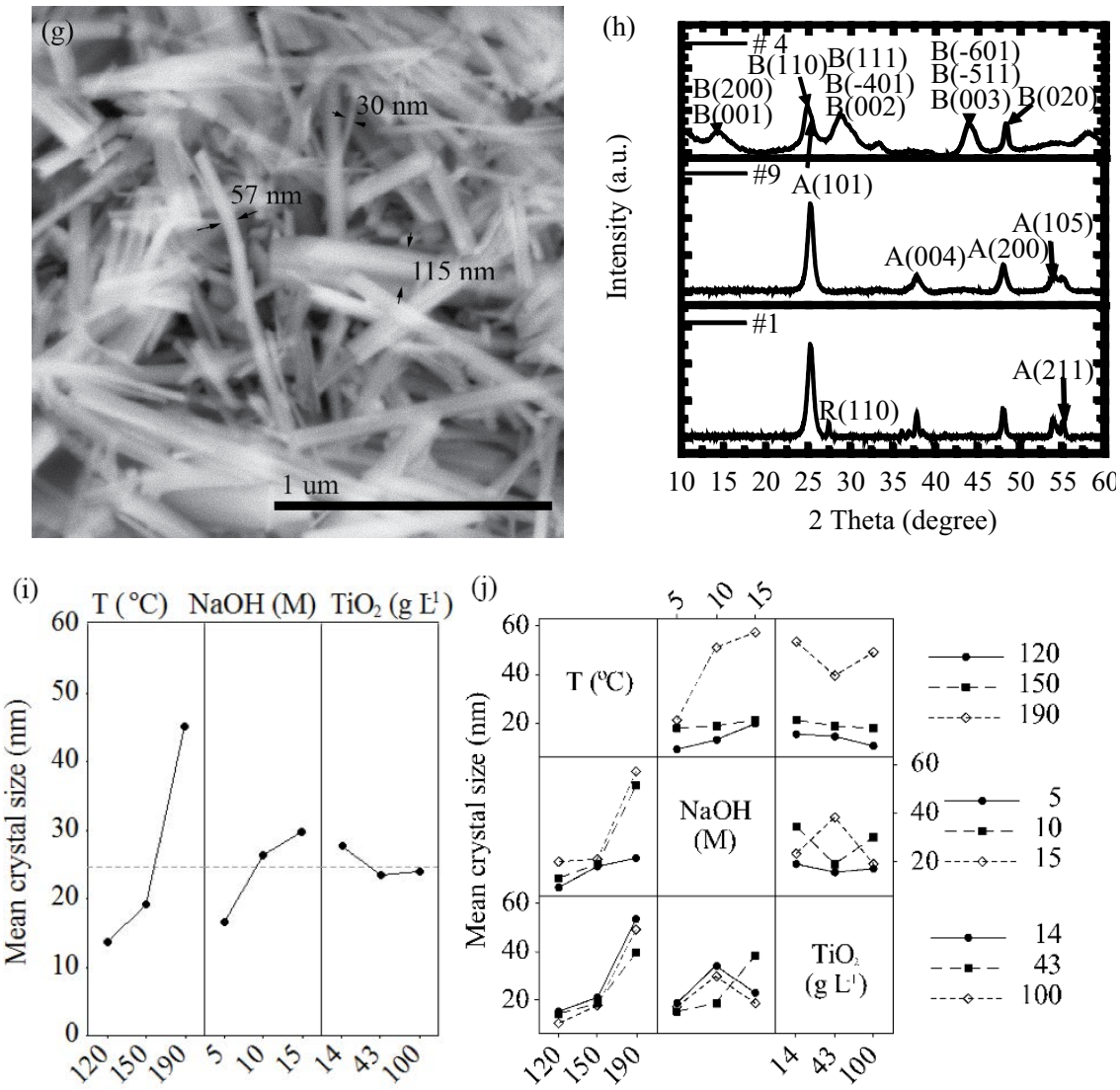

Fig. 1. Morphology, crystal phase, and crystal size of samples: (a) SEM image for sample #9: 150°C, 5 M NaOH, and 14 g L^{-1} TiO_2, (b) TEM image for sample #9, (c) SEM image for sample #2: 190°C, 5 M NaOH, and 43 g L^{-1} TiO_2, (d) SEM image for sample #1: 120°C, 5 M NaOH, and 43 g L^{-1} TiO_2, (e) SEM image for sample #6: 190°C, 10 M NaOH, and 14 g L^{-1} TiO_2, (f) SEM image for sample #8: 190°C, 10 M NaOH, and 100 g L^{-1} TiO_2, (g) SEM image for sample #4: 190°C, 15 M NaOH, and 43 g L^{-1} TiO_2, (h) XRD pattern for samples #1, #4, and #9, (i) main effect of hydrothermal factors on the crystal size of Q1D TiO_2, and (j) interaction plots for the effect of different factors on crystal size of Q1D TiO_2.
Notes: Synthesis parameter details are listed in Table 2. The A(101) peak is positioned on the shoulder. A, R, and B represent anatase, rutile, and TiO_2-B, respectively.

3. Results and discussion

3.1. Q1D TiO_2 physical properties: crystal size, SSA, phase, and bandgap

Significant differences in the Q1D TiO_2 phase structure, crystal size, and SSA were observed under the different hydrothermal conditions. Q1D TiO_2 SEM and HRTEM images for the selected BBD conditions are shown in Figs. 1(a)–(g). The mean diameter of 18 nm (Fig. 1(b)) for sample #9 (150°C, 5 M, and 14 g L^{-1}) with Q1D morphology (Figs. 1(a) and (b)) was smaller when compared with the diameter ranging from 30 to 115 nm for sample #6 (190°C, 15 M, and 43 g L^{-1}), #8 (190°C, 15 M, and 43 g L^{-1}), and #4 (190°C, 15 M, and 43 g L^{-1}) (Figs. 1(e)–(g)). The image for sample #1 (120°C, 5 M, and 43 g L^{-1}) (Fig. 1(d)) shows nanorod with morphologies characteristic of containing shorter length when compared with the other samples. The data indicate the hydrothermal synthesis factors significantly impacted the Q1D TiO_2 diameter and crystal size. The crystal size was investigated using XRD data for all the samples.

XRD analysis was conducted to evaluate the impact of hydrothermal synthesis factors on the crystal size along with the crystal phase. The XRD profiles are shown in Fig. 1(h) for selected BBD samples #1, #4, and #9. The crystal size was calculated for all the samples using Scherrer equation (Eq. (2)). The phase structure and crystal size for all the samples are

Table 3
Phase structures and corresponding bandgap energies for all the BBD samples

Sample #	Phase	Bandgap energy (eV)	Mean crystal size (nm)
1	Anatase–rutile	3.06 ± 0.01	9.3 ± 0.1
2, 3, 5, 7, 9–15	Anatase	3.26 ± 0.01–3.30 ± 0.01	16.8 ± 0.2–57.7 ± 0.4
4, 6, 8	TiO_2-B-anatase	3.20 ± 0.01–3.23 ± 0.01	46.6 ± 0.3–58.9 ± 0.5

listed in Tables 2 and 3. The anatase [28], rutile [29,30], and TiO_2-B [23,31] phases were detected in selected samples with the anatase phase observed in all the Q1D TiO_2 samples. The temperature and NaOH concentration were significant factors affecting the Q1D TiO_2 phase structure. At a relative lower temperature (120°C) and a lower NaOH concentration (5 M), a biphasic anatase–rutile structure was observed in sample #1. Sample #1 was the only experimental design condition with the same biphasic anatase–rutile structure as TiO_2 P25 [6,29,32]. When the temperature was set at 190°C with the NaOH concentration at 10 or 15 M, the TiO_2-B phase was predominant in samples #4, #6, and #8 together with a small quantity of the anatase phase (Fig. 1 and Table 2).

The mean crystal size (L) for different hydrothermal conditions (Table 2 and Figs. 1(e) and (f)) was calculated using Scherrer equation (Eq. (2)) [33].

$$L = \frac{K\lambda}{\beta \times \cos\theta} \tag{2}$$

where K, λ, and β represent the shape factor (0.89), the wavelength of XRD radiation, and the full width at half maximum of peaks, respectively.

The data show the mean crystal size was variable with changes in the synthesis parameter settings. The synthesis temperature and NaOH concentration significantly affected the crystal size, whereas, the TiO_2 precursor concentration had a slight impact on the crystal size. Decreasing crystal size was closely linked with lower temperatures and lower NaOH concentrations. Increasing the hydrothermal temperature from 120°C to 190°C or NaOH concentration from 5 to 15 M resulted in an increase in the average Q1D TiO_2 crystal size from 9.3 ± 0.1 to 58.5 ± 0.3 nm. This observation is consistent with work reported by Bavykin et al. [16].

The high SSA was closely linked to the small crystal sizes of the Q1D TiO_2 nanomaterial. Increasing the SSA is known to increase the photocatalytic activities [6]. Sample #1 with a small mean crystal size of 9.3 ± 0.1 nm represented a high SSA 220 ± 5 $m^2\ g^{-1}$, and sample #9 with an increasing mean crystal size of 16.8 ± 0.2 nm represented a decreasing SSA of 170 ± 3 $m^2\ g^{-1}$, whereas sample #4 with largest mean crystal size of 58.9 ± 0.5 nm had the smallest SSA of 40 ± 2 $m^2\ g^{-1}$.

Diffuse reflectance UV-Vis spectroscopy for P25 nanoparticles and selected Q1D TiO_2 samples are shown in Fig. 2. All the samples showed a wide optical absorption below a critical value of approximately 410 nm [34]. This broad band can be assigned to the band–band electron transition of the TiO_2 nanocrystals based on its bandgap energy [29,34]. Notice with decreasing hydrothermal temperatures, the absorption band edges (Fig. 2(a)) for sample #1 with a biphasic anatase–rutile structure gradually shifted toward longer wavelengths. The data clearly indicate the ability of Q1D TiO_2 to absorb UV light increased with decreasing hydrothermal temperatures. The Kubelka-Munk function was used to transform the diffuse reflectance spectra into the corresponding absorption spectra (Fig. 2(b)) [35]. In this study, the bandgap energies for

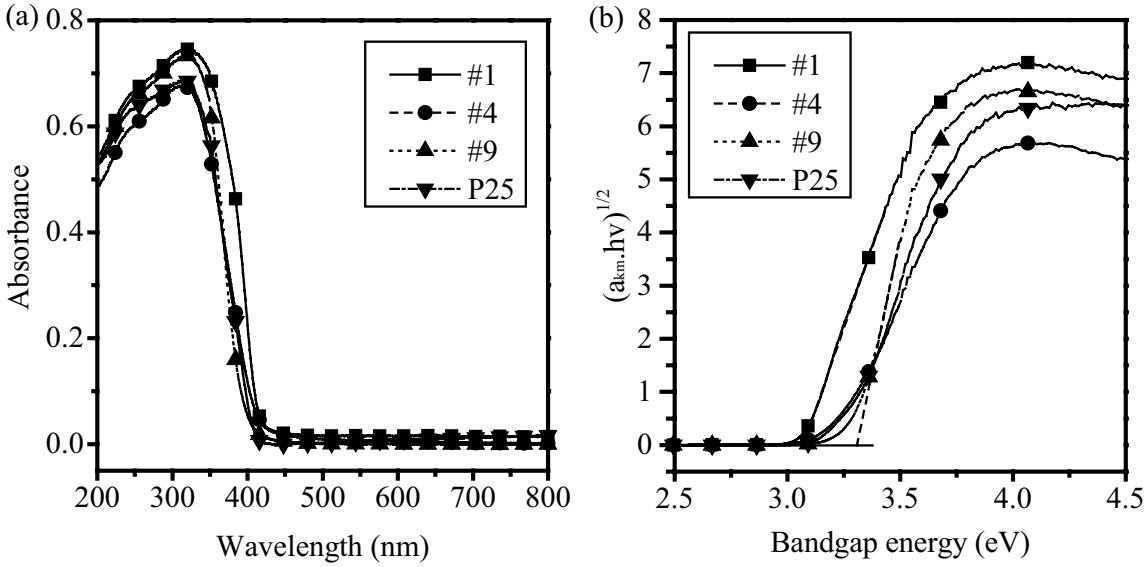

Fig. 2. Plots of (a) diffuse reflectance UV-Vis spectroscopy and (b) $(a_{km}hv)^{1/2}$ versus the energy absorbed for BBD samples (Table 2).

the 15 BBD samples ranging from 3.07 to 3.30 eV were closely related to the crystal phase (Table 3). Table 3 lists the phase structures and corresponding bandgap energies for samples #1 to #15. Pure anatase samples (e.g., sample #9) had the largest bandgap energy close to 3.30 eV [36,37]. The lower band gap energy for the biphasic anatase–rutile (sample #1) and biphasic TiO2-B-anatase (samples #4, #6, and #8) structures were 3.06 and 3.23 eV, respectively. Interestingly, the smaller bandgap energy of 3.06 eV for the sample #1 was due to the existence of the rutile phase with a bandgap value of 3.01 eV [30]. Sample #1 with lower bandgap energies has the ability to absorb more radiation with a subsequent enhancement in photocatalytic activities [38].

3.2. RhB photocatalysis

Under the different hydrothermal factors, the Q1D TiO_2 samples showed differences in the photocatalytic efficiency with respect to the discoloration or disappearance of RhB. Profiles for the residual RhB concentration versus time and the corresponding apparent reaction rate constant, k ($kt = -\ln(C/C_o)$), are shown in Fig. 3 for selected samples (Table S1). Control experiments were performed with P25 nanoparticles and without the P25 photocatalyst. The average apparent RhB photocatalysis rate constant value (designated as "apparent RhB k") was 0.0030 ± 0.0001 min^{-1} without a photocatalyst; however, with the addition of P25 nanoparticles, the average value increased to 0.3483 ± 0.0051 min^{-1}. Only the Q1D TiO_2 photocatalyst synthesized under conditions designated as #1 (120°C, 5 M NaOH, and 43 g L^{-1} TiO_2) showed the apparent RhB k value (0.4227 ± 0.0107 min^{-1}) larger than the value for the TiO_2 P25 photocatalyst (Table S1 and Fig. 3). The average apparent RhB k value for the sample #4 and sample #9 were 0.0936 ± 0.0007 and 0.2569 ± 0.0039 min^{-1}, respectively. Depending on the hydrothermal synthesis conditions, the average apparent reaction rate constant value, k, varied from 0.0936 ± 0.0007 to 0.4227 ± 0.0107 min^{-1} (Table 2). For sample #1, the enhanced RhB photocatalytic activity was due to the formation of the active biphasic anatase–rutile structure [6,39] with the Q1D nanostructure [9,40] synthesized under relatively lower synthesis temperature of 120°C and lower NaOH concentration of 5 M. The lowest photocatalytic activity was detected for sample #4 containing the TiO_2-B phase. Based on the apparent reaction rate constants, the hydrothermal synthesis conditions significantly affected the photocatalytic activity.

3.3. Modeling and optimization of hydrothermal synthesis

The impact of varying the hydrothermal synthesis factors, namely temperature, NaOH concentration, and the TiO_2 concentration (Fig. S1) is crucial for optimizing the Q1D TiO_2 photocatalytic activity. Optimization using a "one-factor-at-a-time" (OFAT) approach is tedious and time-consuming. Furthermore, the OFAT method is unable to account for interactions between the various hydrothermal synthesis factors. In this study, response surface methodology was utilized to evaluate the impacts of various hydrothermal synthesis factors on the Q1D TiO_2 photocatalytic activity.

A multiple regression analysis was used to develop a quadratic Eq. (3). Eq. (3) describes the apparent reaction rate constant (k) for RhB photocatalysis or the apparent RhB k as a function of the hydrothermal process factors.

$$\begin{aligned} k = {} & 1.184 - 0.00665A - 0.0520B - 0.00102C + \\ & 0.000041AB + 0.000014AC + 0.000103BC + \\ & 0.000013A^2 + 0.001296B^2 - 0.000014C^2 \end{aligned} \tag{3}$$

where k (min^{-1}) is the apparent RhB rate constant and A, B, and C represents the hydrothermal synthesis temperature (°C), NaOH concentration (M), and TiO_2 concentration ($g \cdot L^{-1}$), respectively (Table 1).

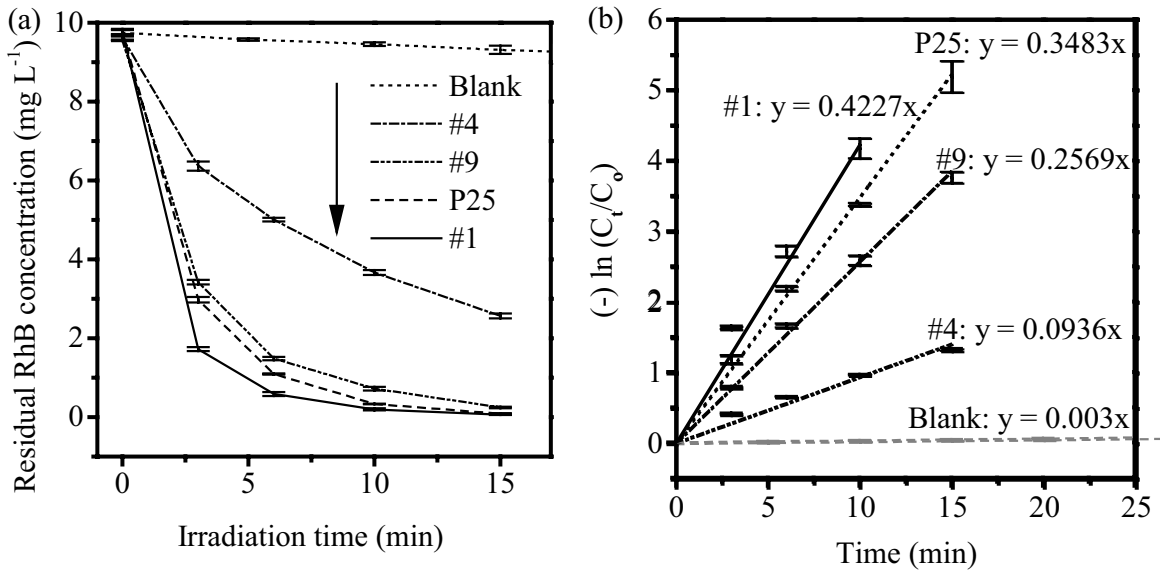

Fig. 3. RhB photocatalysis concentration profiles and kinetic plots for selected samples. (a) RhB photocatalysis concentration profiles using 300 nm UV light and (b) apparent reaction rate constant.
Note: BBD conditions are shown in Table 2. Blank represents no photocatalyst.

The three-dimensional response surface and the corresponding contour plots of experimental factors with the apparent RhB k are shown in Fig. 4. The response surface plots show interaction between temperature and NaOH concentration (Figs. 4(a) and (b)) with larger k values observed at lower temperatures and lower NaOH concentrations. The larger k value was associated with a biphasic anatase–rutile phase structure, which showed the lowest bandgap energy and smallest crystal size of 9.3 ± 0.1 nm. The enhanced photocatalytic activities of biphasic anatase–rutile were due to the increasing photogenerated holes and electrons separation between the anatase and rutile phases [6,39]. Supporting work [39] employing surface-enhanced Raman spectroscopy has shown that mixed crystal TiO_2 structures with an appropriate proportion of anatase and rutile phase is favorable towards efficient charge transfer and separation. Increasing reaction temperature and NaOH concentration was closely linked to 100% anatase phase and decreasing k values. When the temperature was set at 190°C with the NaOH concentration at 10 or 15 M, the Q1D TiO_2 containing TiO_2-B phase was correlated with a significantly low k value. The negative effect of TiO_2-B on RhB photodegradation rate is contrary to the observed positive effect of TiO_2-B reported by Zhang et al. [41].

Increasing k values were observed at lower temperatures and TiO_2 concentrations of approximately 35 g L^{-1} (Figs. 4(c) and (d)). The photocatalytic activity of the Q1D TiO_2 structure was slightly affected by the TiO_2 precursor concentration. Enhancing the k value could be achieved at a TiO_2 concentration of 35 g L^{-1}. Interactions between the NaOH and TiO_2 concentrations (Figs. 4(e) and (f)) confirmed that a low NaOH concentration and an appropriate TiO_2 concentration of approximately 35 g L^{-1} TiO_2 were important factors causing an increase in the k value.

Locating the region of maximum response (apparent RhB k) was conducted using the D-optimality index. Within the factor space under consideration, the D-optimality index was determined using the Minitab® software optimization function. The D-optimality index range from 0 to 1 represents the ideal and worst cases, respectively. The D-optimality plot for the apparent RhB k for all the different factors beginning from the low factor-level setting is shown in Fig. 5. A D-optimality value of 0.8990 with a maximum photocatalysis rate (response) of 0.4412 min^{-1} was determined under conditions set at 120°C, 5 M NaOH, and 26.0 g L^{-1} TiO_2. Additional experiments were conducted to verify the optimum k value under the optimized hydrothermal conditions at 120°C, 5 M NaOH, and 26.0 g L^{-1} TiO_2. The predicted value was slightly underestimated when compared with the observed k of 0.4506 ± 0.0167 min^{-1}. The apparent RhB k for Q1D TiO_2 synthesized using the optimized conditions was approximately 30% larger when compared with the commercial P25.

3.4. Response surface model development

An analysis of variance (ANOVA) was employed to evaluate the model full quadratic Eq. (3) to determine the significance and adequacy of the model (Table 4). Terms with a p-value less than 0.05 are statistically significant, whereas the terms with a p-value greater than 0.05 are insignificant [42–45]. A p-value of 0 (less than 0.05) and F-value (24.46) less than F-critical value (2.01 at 5% level of significance) for the model indicates that the quadratic model is statistically significant since most of the terms are significant. The F-value of 24.46 for model was greater than the F-critical value of 2.01 (at 5% level of significance) [42–45]. However, temperature (°C) × temperature (°C) and temperature (°C) × NaOH concentration (M) with p-value larger than 0.05 are statistically insignificant, indicating these two variables had no individual effect on the response (Eq. (3)). Statistically insignificant terms in the full quadratic model were deleted using a backward elimination method [43]. The final response surface model is designated as Eq. (4):

$$k = 0.8 - 0.002081A - 0.04479B - 0.00092C + 0.000014AC + 0.000102BC + 0.001247B^2 - 0.000023C^2 \quad (4)$$

where k (min^{-1}) is the apparent RhB photocatalytic rate constant and A, B, and C represents temperature (°C), NaOH concentration (M), and TiO_2 concentration (g L^{-1}), respectively. All the terms are statistically significant in Eq. (4).

3.5. Response surface model verification

A scatter plot of the experimental values and predicted values from the model equation demonstrated a reasonable correlation for each level (Fig. 6(a)). Assessing the adequacy of fitting the model to experimental data was conducted using the Anderson–Darling (AD) statistic. The AD statistic was employed to determine the normal distribution of the residuals (difference between the predicted and experimentally apparent photocatalysis rate constant) (Fig. 6(b)) [46]. The AD value (0.231) was below the critical value of the statistic (0.735) for a sample size of 45 and at a 5% level of significance [46,47]. A p-value (0.793) greater than 0.05 suggest the model prediction fitted reasonably well with the experimental data.

Additional experiments were conducted to validate the accuracy of the model within the experimental factors under examination. Each of the three factors was evaluated by employing a separate validation study. The model prediction was in agreement with the experimental results for the temperature ranging from 120°C to 190°C (Fig. 7(a)), although the model slightly underestimated and overestimated the apparent RhB k at 150°C and 190°C, respectively. For the NaOH concentration, the predicted points were consistent with the experimental points with a slight overestimate at 5 M NaOH (Fig. 7(b)). For the TiO_2 concentration, the predicted values were slightly underestimated compared with the observed values for each level of TiO_2 concentration (Fig. 7(c)). Notably, the trend for varying temperature, the NaOH and TiO_2 concentrations were in agreement with the experimental observations.

3.6. Photocatalysis of other chemicals using the optimized Q1D TiO_2

The Q1D TiO_2 produced under the optimized conditions was also employed to photodegrade phenol, MO, and MB (Fig. 8). The apparent k value for each chemical is shown in Figs. 8(a)–(c). The data set trend for the apparent k clearly shows that Q1D TiO_2 synthesized under decreasing temperature conditions (e.g., optimized Q1D TiO_2 and sample #1) were correlated with larger k values. The largest k value

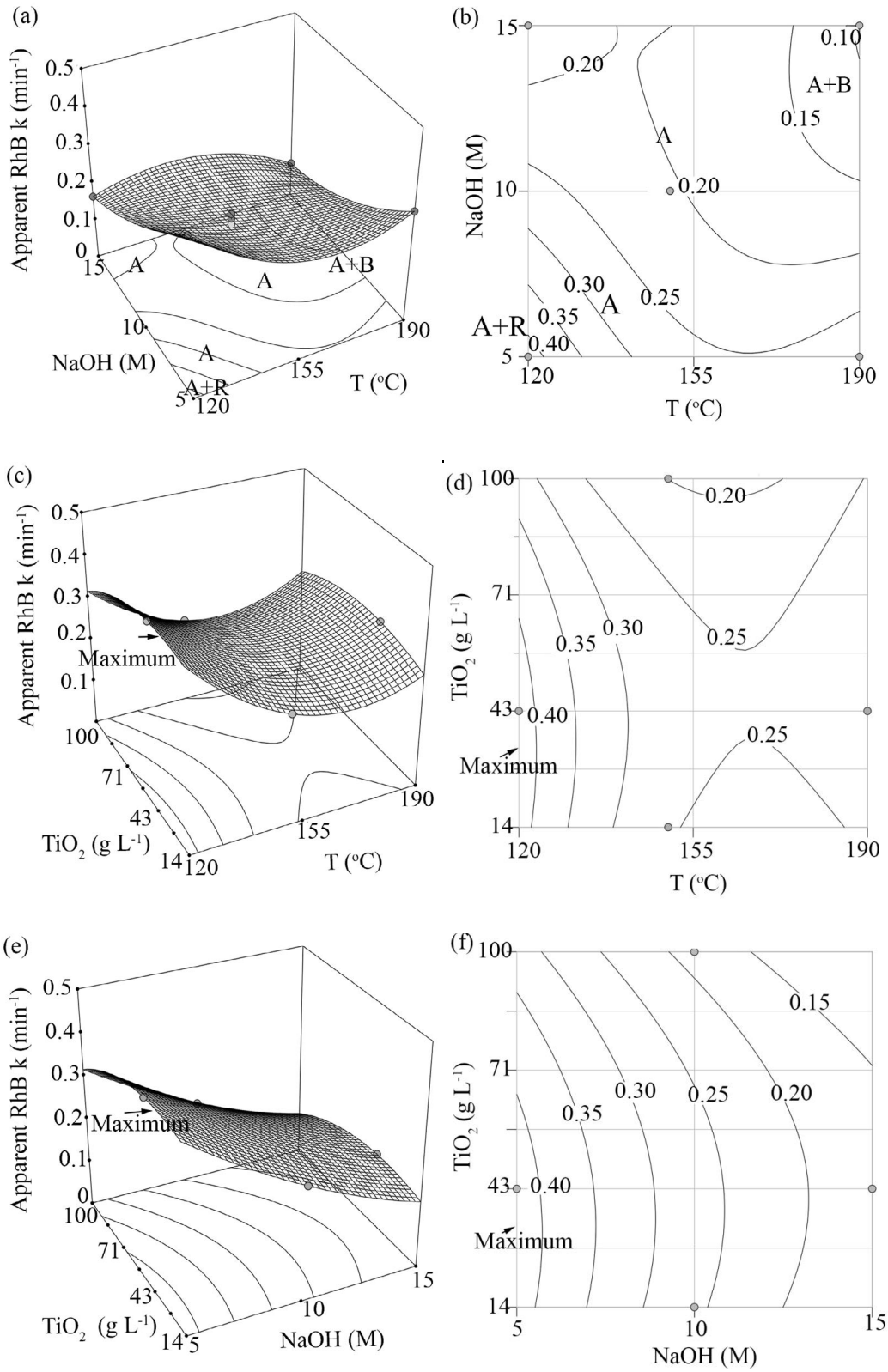

Fig. 4. Response surface and contour plots for factors affecting the apparent RhB rate constant (min^{-1}). (a) and (b) hydrothermal temperature and NaOH concentration set at 43 g L^{-1} TiO_2, (c) and (d) hydrothermal temperature and TiO_2 concentration set at 5 M NaOH concentration, (e) and (f) NaOH concentration and TiO_2 concentration set at 120°C temperature.
Note: Apparent RhB *k* represents the "apparent rhodamine B photocatalysis rate constant value" and A, B, and R represent anatase, TiO_2-B, and rutile phases, respectively.

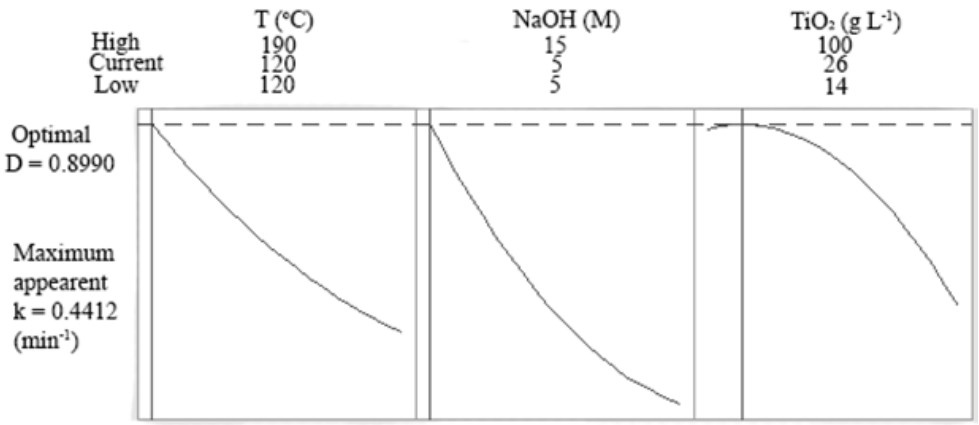

Fig. 5. Optimality plot to locate optimum factor levels for maximized response k (min^{-1}).

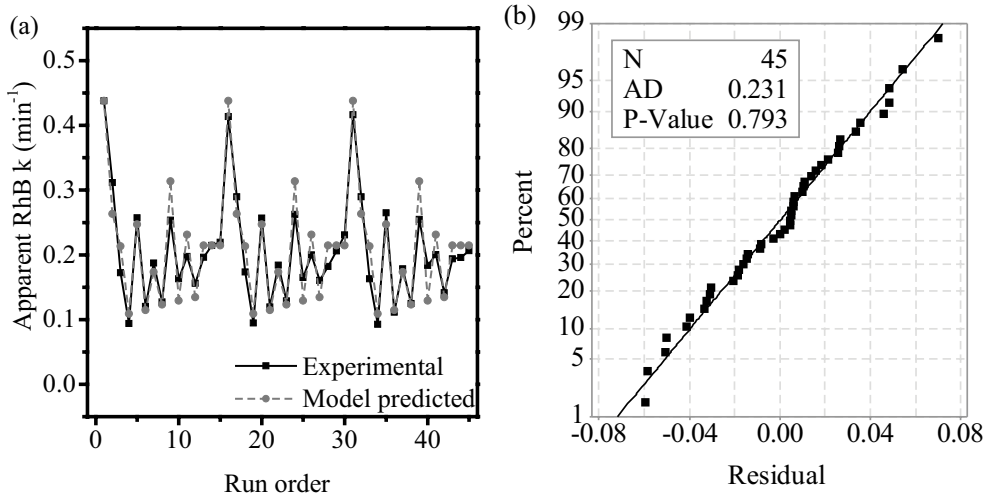

Fig. 6. Evaluating accuracy of the response surface model. (a) Scatter plot of the apparent RhB k versus experiment order (45 experiments). (b) Anderson–Darling normality plot of residuals.
Notes: N = the number of experiments conducted in this study; p-value = level of confidence; AD = Anderson–Darling statistic.

Table 4
ANOVA results of the experimental response at each factor level

Source	DF[1]	Seq. SS[2]	MS[3]	F-Value	p-Value
Model	9	0.24459	0.02718	24.46	0
A	1	0.04991	0.04991	44.91	0
B	1	0.10955	0.10955	98.58	0
C	1	0.00632	0.00632	5.69	0.023
A^2	1	0.00281	0.00281	2.53	0.121
B^2	1	0.01163	0.01163	10.46	0.003
C^2	3	0.01389	0.01389	12.50	0.001
AB	1	0.00062	0.00062	0.56	0.46
AC	1	0.00535	0.00535	4.82	0.035
BC	1	0.00617	0.00617	5.55	0.024
Error	35	0.03889	0.00111		
Total	44	0.28348			

Notes: DF = degrees of freedom, Seq. SS = sequential sum of square, MS = mean square, A = temperature, B = NaOH concentration, C = TiO_2 concentration.

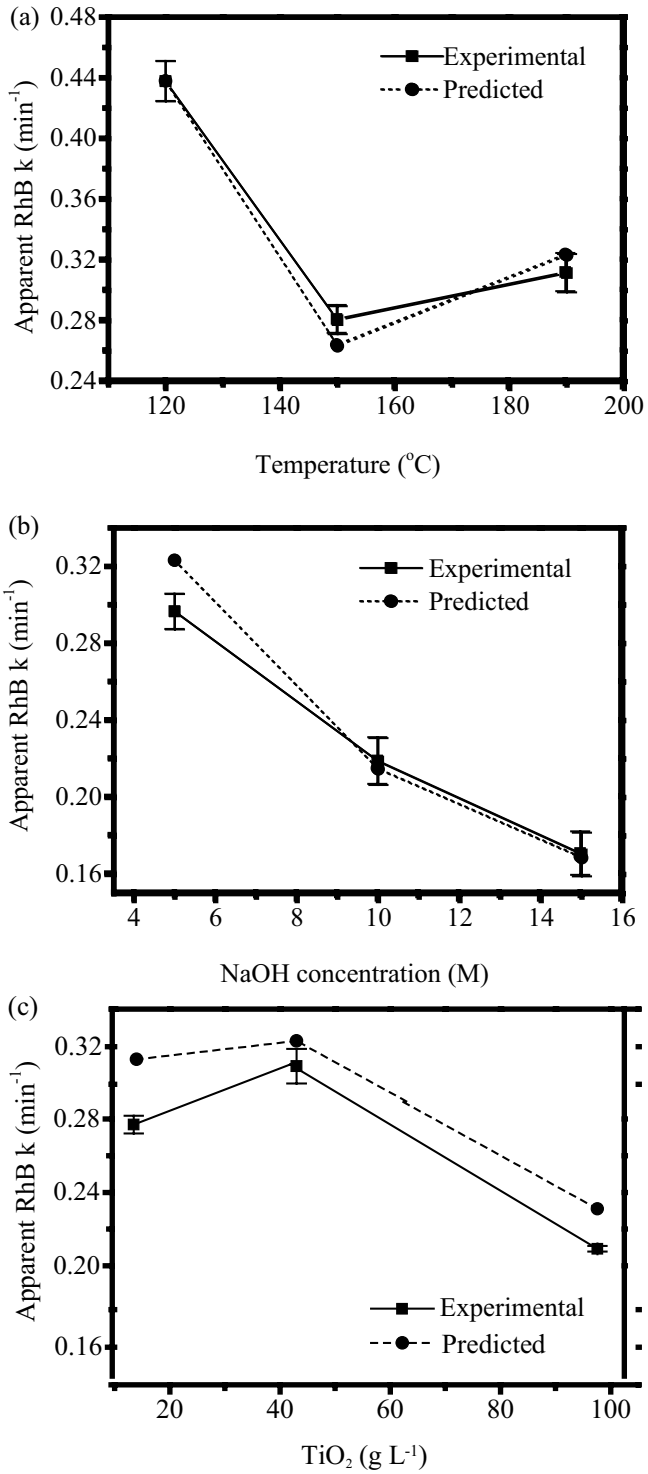

Fig. 7. Validation study of the response surface model for the varied factors under consideration. (a) Apparent RhB *k* value versus temperature at experimental conditions set at 5 M NaOH and 43 g L^{-1} TiO_2, (b) apparent RhB *k* versus NaOH concentration at experimental conditions set at 150°C and 43 g L^{-1} TiO_2, and (c) apparent RhB *k* value versus TiO_2 concentration at experimental conditions set at 150°C and 5 M NaOH.

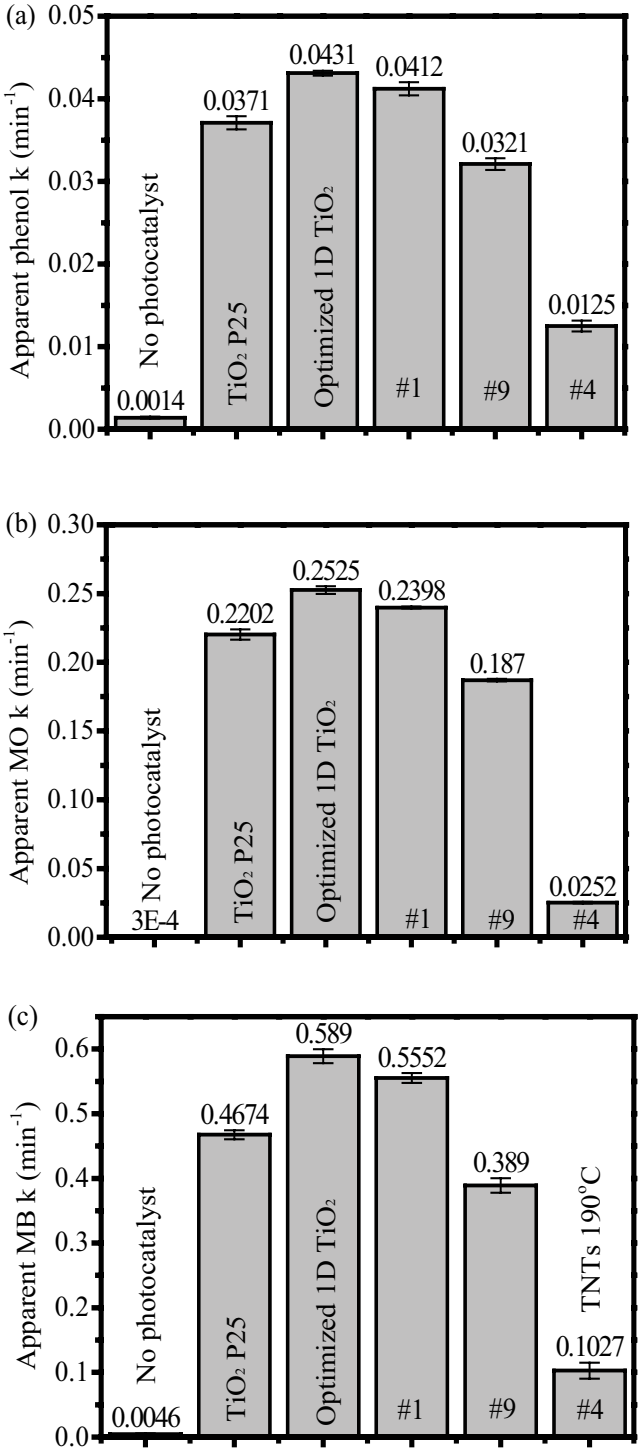

Fig. 8. Apparent rate constant for the different organic chemicals and selected photocatalysts: (a) phenol, (b) methyl orange, and (c) methylene blue.

Notes: Optimized Q1D TiO_2 was synthesized at 120°C, 5 M NaOH, and 26 g L^{-1} TiO_2, other samples synthesis conditions are listed in Table 2.

was observed for the optimized Q1D TiO_2. The apparent *k* for phenol, MO, and MB when using the optimized Q1D TiO_2 was 1.16, 1.24, and 1.26-fold, respectively, greater than that of the P25 nanoparticles photocatalyst. The data indicate that the optimized Q1D TiO_2 is a promising photocatalyst for degrading organic chemicals when compared with P25. Sample #4 small apparent k for each chemical clearly indicates TiO_2-B exerted a negative influence on the photocatalytic activity.

4. Conclusions

A statistical model was developed to evaluate the effects of the hydrothermal synthesis factors on the photocatalytic activity of Q1D TiO_2 based on RhB photocatalysis. The AD statistic indicated an adequate fit of the statistical model to the experimental data. The model predicted a maximum apparent photocatalytic rate constant was achieved using a biphasic anatase–rutile photocatalyst synthesized at 120°C, 5 M NaOH, and 26 g L^{-1} TiO_2. The biphasic anatase–rutile structure was favorable for photocatalysis of RhB and other chemicals. The TiO_2-B phase was produced using a relatively high temperature of 190°C and relatively high NaOH concentrations between 10 and 15 M. This study demonstrated that the TiO_2-B phase negatively affected the photocatalysis of selected chemicals. When using the optimized biphasic anatase–rutile Q1D TiO_2, the apparent photocatalysis rate constant for phenol, MO, and MB under UV light conditions were enhanced by three- to five fold in comparison with using TiO_2-B. The study also demonstrated that optimum photodegrading activity was observed for a selected Q1D TiO_2 photocatalyst containing phase structure and crystal size which were controlled by the synthesis conditions.

Acknowledgments

Financial support for this work was provided by the Natural Sciences and Engineering Research Council (NSERC) of Canada (grant # 261797-2009), the Ontario Trillium scholarship program, and the University of Windsor (grant #13320).

References

[1] P. Bansal, N. Bhullar, D. Sud, Studies on photodegradation of malachite green using TiO_2/ZnO photocatalyst, Desal. Wat. Treat., 12 (2012) 108–113.
[2] X. Liu, T. Lv, Y. Liu, L. Pan, Z. Sun, TiO_2–Au composite for efficient UV photocatalytic reduction of Cr(VI), Desal. Wat. Treat., 51 (2013) 3889–3895.
[3] Q. Han, Y. Wang, H. Yan, B. Gao, D. Ma, S. Sun, J. Ling, Y. Chu, Photocatalysis of THM precursors in reclaimed water: the application of TiO_2 in UV irradiation, Desal. Wat. Treat., 57 (2016) 9136–9147.
[4] A. Mezni, N.B. Saber, M.M. Ibrahim, M. El-Kemary, A. Aldalbahi, P. Feng, L. Samia Smiri, T. Altalhi, Facile synthesis of highly thermally stable TiO_2 photocatalysts, New J. Chem., 41 (2017) 5021–5027.
[5] S. Ray, J.A. Lalman, Fabrication and characterization of an immobilized titanium dioxide (TiO_2) nanofiber photocatalyst, Mater. Today, Proc., 3 (2016) 1582–1591.
[6] G. Tian, H. Fu, L. Jing, B. Xin, K. Pan, Preparation and characterization of stable biphase TiO_2 photocatalyst with high crystallinity, large surface area, and enhanced photoactivity, J. Phys. Chem. C, 112 (2008) 3083–3089.
[7] Y. Yu, P. Zhang, L. Guo, Z. Chen, Q. Wu, Y. Ding, W. Zheng, Y. Cao, The design of TiO_2 nanostructures (nanoparticle, nanotube, and nanosheet) and their photocatalytic activity, J. Phys. Chem. C, 118 (2014) 12727.
[8] J.G. Lu, P. Chang, Z. Fan, Quasi-one-dimensional metal oxide materials – synthesis, properties and applications, Mater. Sci. Eng., R, 52 (2006) 49–91.
[9] X. Pan, Y. Zhao, S. Liu, C.L. Korzeniewski, S. Wang, Z. Fan, Comparing graphene-TiO_2 nanowire and graphene-TiO_2 nanoparticle composite photocatalysts, ACS Appl. Mater. Interfaces, 4 (2012) 3944–3950.
[10] S.D. Perera, R.G. Mariano, K. Vu, N. Nour, O. Seitz, Y. Chabal, K.J. Balkus Jr., Hydrothermal synthesis of graphene-TiO_2 nanotube composites with enhanced photocatalytic activity, ACS Catal., 2 (2012) 949–956.
[11] G. Wang, H. Wang, Y. Ling, Y. Tang, X. Yang, R.C. Fitzmorris, C. Wang, J.Z. Zhang, Y. Li, Hydrogen-treated TiO_2 nanowire arrays for photoelectrochemical water splitting, Nano Lett., 11 (2011) 3026–3033.
[12] X. Kang, S. Chen, Photocatalytic reduction of methylene blue by TiO_2 nanotube arrays: effects of TiO_2 crystalline phase, J. Mater. Sci., 45 (2010) 2696–2702.
[13] M. Fathy, H. Hamad, A. El Hady Kashyout, Influence of calcination temperatures on the formation of anatase TiO_2 nano rods with a polyol-mediated solvothermal method, RSC Adv., 6 (2016) 7310–7316.
[14] T. Kasuga, M. Hiramatsu, A. Hoson, T. Sekino, K. Niihara, Formation of titanium oxide nanotube, Langmuir, 14 (1998) 3160–3163.
[15] Y. Tang, Y. Zhang, J. Deng, J. Wei, H.L. Tam, B.K. Chandran, Z. Dong, Z. Chen, X. Chen, Mechanical force-driven growth of elongated bending TiO_2-based nanotubular materials for ultrafast rechargeable lithium ion batteries, Adv. Mater., 26 (2014) 6111–6118.
[16] D.V. Bavykin, V.N. Parmon, A.A. Lapkin, F.C. Walsh, The effect of hydrothermal conditions on the mesoporous structure of TiO_2 nanotubes, J. Mater. Chem., 14 (2004) 3370–3378.
[17] B.-M. Wen, C.-Y. Liu, Y. Liu, Solvothermal synthesis of ultralong single-crystalline TiO_2 nanowires, New J. Chem., 29 (2005) 969–971.
[18] S. Hoang, S. Guo, N.T. Hahn, A.J. Bard, C.B. Mullins, Visible light driven photoelectrochemical water oxidation on nitrogen-modified TiO_2 nanowires, Nano Lett., 12 (2012) 26–32.
[19] P. Roy, S. Berger, P. Schmuki, TiO_2 nanotubes: synthesis and applications, Angew. Chem. Int. Ed., 50 (2011) 2904–2939.
[20] Y.V. Kolen'ko, K.A. Kovnir, A.I. Gavrilov, Hydrothermal synthesis and characterization of nanorods of various titanates and titanium dioxide, J. Phys. Chem. B, 110 (2006) 4030–4038.
[21] J.-N. Nian, H. Teng, Hydrothermal synthesis of single-crystalline anatase TiO_2 nanorods with nanotubes as the precursor, J. Phys. Chem. B, 110 (2006) 4193–4198.
[22] Z. Yang, B. Wang, H. Cui, H. An, Y. Pan, J. Zhai, Synthesis of crystal-controlled TiO_2 nanorods by a hydrothermal method: rutile and brookite as highly active photocatalysts, J. Phys. Chem. C, 119 (2015) 16905–16912.
[23] H.-L. Kuo, C.-Y. Kuo, C.-H. Liu, J.-H. Chao, C.-H. Lin, A highly active bi-crystalline photocatalyst consisting of TiO_2 (B) nanotube and anatase particle for producing H_2 gas from neat ethanol, Catal. Lett., 113 (2007) 7.
[24] S. Ray, J.A. Lalman, N. Biswas, Using the Box-Benkhen technique to statistically model phenol photocatalytic degradation by titanium dioxide nanoparticles, Chem. Eng. J., 150 (2009) 15–24.
[25] D. Yang, Y. Sun, Z. Tong, Y. Tian, Y. Li, Synthesis of Ag/TiO_2 nanotube heterojunction with improved visible-light photocatalytic performance inspired by bioadhesion, J. Phys. Chem. C, 119 (2015) 5827–5835.
[26] D. Xu, B. Cheng, S. Cao, J. Yu, Enhanced photocatalytic activity and stability of Z-scheme Ag_2CrO_4-GO composite photocatalysts for organic pollutant degradation, Appl. Catal., B, 164 (2015) 380–388.
[27] M. Nasr, R. Viter, C. Eid, R. Habchi, P. Miele, M. Bechelany, Enhanced photocatalytic performance of novel electrospun BN/TiO_2 composite nanofibers, New J. Chem., 41 (2016) 81–89.
[28] H. Cheng, J. Ma, Z. Zhao, L. Qi, Hydrothermal preparation of uniform nanosize rutile and anatase particles, Chem. Mater., 7 (1995) 663–671.

[29] H. Zhang, J.F. Banfield, Understanding polymorphic phase transformation behavior during growth of nanocrystalline aggregates: insights from TiO_2, J. Phys. Chem. B, 104 (2000) 3481–3487.
[30] D. Reyes-Coronado, G. Rodriguez-Gattorno, M.E. Espinosa-Pesqueira, C. Cab, R. de Coss, G. Oskam, Phase-pure TiO_2 nanoparticles: anatase, brookite and rutile, Nanotechnology, 19 (2008) 145605.
[31] T.P. Feist, P.K. Davies, The soft chemical synthesis of TiO_2 (B) from layered titanates, J. Solid State Chem., 101 (1992) 275–295.
[32] M.C. Hidalgo, M. Maicu, J.A. Navío, G. Colón, Photocatalytic properties of surface modified platinised TiO_2: effects of particle size and structural composition, Catal. Today, 129 (2007) 43–49.
[33] A. Monshi, M.R. Foroughi, M.R. Monshi, Modified Scherrer equation to estimate more accurately nano-crystallite size using XRD, World J. Nano Sci. Eng., 02 (2012) 154–160.
[34] H. Luo, C. Wang, Y. Yan, Synthesis of mesostructured titania with controlled crystalline framework, Chem. Mater., 15 (2003) 3841–3846.
[35] R. Lopez, R. Gomez, Band-gap energy estimation from diffuse reflectance measurements on sol–gel and commercial TiO_2: a comparative study, J. Sol-Gel Sci. Technol., 61 (2012) 1–7.
[36] J. Tao, T. Luttrell, M. Batzill, A two-dimensional phase of TiO_2 with a reduced bandgap, Nat. Chem., 3 (2011) 296–300.
[37] W. Fan, Q. Lai, Q. Zhang, Y. Wang, Nanocomposites of TiO_2 and reduced graphene oxide as efficient photocatalysts for hydrogen evolution, J. Phys. Chem. C, 115 (2011) 10694–10701.
[38] U. Diebold, Photocatalysts: closing the gap, Nat. Chem., 3 (2011) 271–272.
[39] L. Yang, M. Gong, X. Jiang, D. Yin, X. Qin, B. Zhao, W. Ruan, Investigation on SERS of different phase structure TiO_2 nanoparticles, J. Raman Spectrosc., 46 (2015) 287–292.
[40] S. Hoang, S.P. Berglund, N.T. Hahn, A.J. Bard, C.B. Mullins, Enhancing visible light photo-oxidation of water with TiO_2 nanowire arrays via cotreatment with H_2 and NH_3: synergistic effects between Ti^{3+} and N, J. Am. Chem. Soc., 134 (2012) 3659–3662.
[41] L. Zhang, W. Zheng, H. Jiu, W. Zhu, G. Qi, Preparation of the anatase/TiO_2(B) TiO_2 by self-assembly process and the high photodegradable performance on RhB, Ceram. Int., 42 (2016) 12726–12734.
[42] S.S. Veeravalli, S.R. Chaganti, J.A. Lalman, D.D. Heath, Optimizing hydrogen production from a switchgrass steam exploded liquor using a mixed anaerobic culture in an upflow anaerobic sludge blanket reactor, Int. J. Hydrogen Energy, 39 (2014) 3160–3175.
[43] S.R. Shanmugam, S.R. Chaganti, J.A. Lalman, D.D. Heath, Statistical optimization of conditions for minimum H_2 consumption in mixed anaerobic cultures: effect on homoacetogenesis and methanogenesis, Int. J. Hydrogen Energy, 39 (2014) 15433–15445.
[44] Z. Lai, M. Zhu, X. Yang, J. Wang, S. Li, Optimization of key factors affecting hydrogen production from sugarcane bagasse by a thermophilic anaerobic pure culture, Biotechnol. Biofuels, 7 (2014) 131–111.
[45] A. Reungsang, S. Pattra, S. Sittijunda, Optimization of key factors affecting methane production from acidic effluent coming from the sugarcane juice hydrogen fermentation process, Energies, 5 (2012) 4746–4757.
[46] M.A. Stephens, EDF statistics for goodness of fit and some comparisons, J. Am. Stat. Assoc., 69 (1974) 730.
[47] D.C. Montgomery, Design and Analysis of Experiments, John Wiley and Sons, Inc., Arizona State University, Arizona, 2017.

Supplementary information

1. Impact of hydrothermal conditions on the apparent RhB k

The main effects plot showing the impact of three hydrothermal synthesis factors on the response apparent RhB *k* is illustrated in Fig. S1(a). Increasing the apparent RhB *k* was observed with decreasing temperatures to 120°C. A similar trend was observed with decreasing NaOH levels; however, with increasing TiO_2 concentration to 43 g L^{-1}, the apparent RhB *k* increased and reached a peak value. The apparent RhB *k* value decreased with further increasing the TiO_2 precursor concentration from 43 to 100 g L^{-1} TiO_2. The interaction plots (Fig. S1(b)) indicate a similar pattern as shown in the main effect plot. A larger apparent RhB *k* value was obtained at lower temperatures as well as lower NaOH concentration and with the TiO_2 level set at 43 g L^{-1}.

Table S1
Apparent RhB *k* values for selected samples

Experiment	Apparent reaction rate constant *k* (min^{-1})	Linear regression R^2 value
Control (no photocatalyst)	0.0030 ± 0.0002	0.9991
P25	0.3483 ± 0.0051	0.9823
#1[a]	0.4227 ± 0.0037	0.9729
#4[a]	0.0936 ± 0.0010	0.9674
#9[a]	0.2569 ± 0.0039	0.9740

[a]The reaction conditions are listed in Table 2.

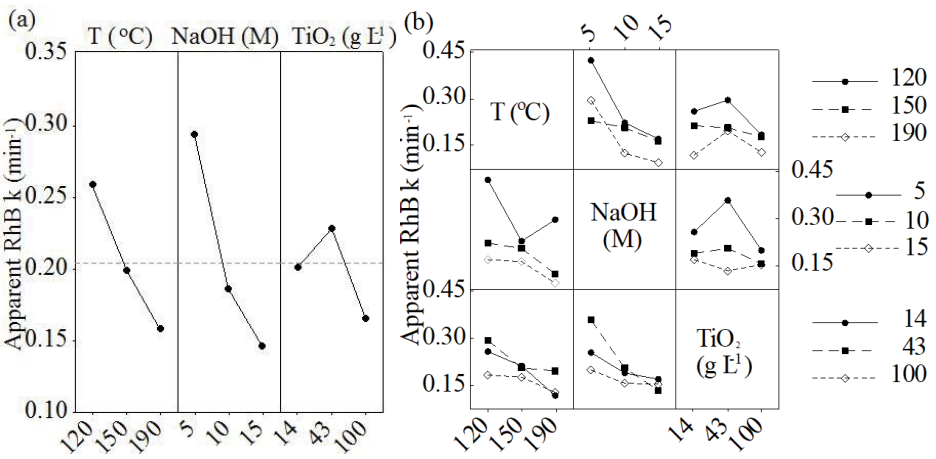

Fig. S1. Main effects (a) and interaction (b) plots for the different experimental factors.
Note: *T* = temperature; NaOH = NaOH concentration, and TiO_2 = TiO_2 concentration.